Journal of Materials Chemistry C

ROYAL SOCIETY OF CHEMISTRY

PAPER

View Article Online
View Journal | View Issue

Cite this: J. Mater. Chem. C, 2025, 13, 5241

Contorted graphene nanoribbons from vat dyes: synthesis, properties and charge carrier mobility†

Ali Darvish,[a] Madison Mooney,[b] Tiago C. Gomes,[b] Félix Gagnon,[a] Simon Rondeau-Gagné[b] and Jean-François Morin*[a]

Received 28th November 2024,
Accepted 15th January 2025

DOI: 10.1039/d4tc05043f

rsc.li/materials-c

Vat dyes represent an interesting class of building blocks for organic electronics as they are readily available at low cost and easy to functionalize. Yet, these molecules have never been used to prepare graphene nanoribbons (GNRs). Using the Brønsted acid-catalyzed alkyne benzannulation, two contorted GNRs have been synthesized from vat orange 1 and vat orange 3 in a few synthetic steps. These GNRs absorb light in the visible region with bandgap values around 2.0 eV and have been tested in organic field-effect transistors (OFETs) to measure their charge transport ability. Hole mobility values of up to 1.34×10^{-2} cm^2 V^{-1} s^{-1} were measured in a bottom-gate top-contact device architecture.

Introduction

Graphene has attracted lots of attention in various areas since its discovery in 2004 due to its remarkable properties such as its exceptional electrical conductivity,[1,2] high thermal conductivity,[3,4] mechanical strength and quantum Hall effect.[5,6] However, its semi-metallic nature (zero-band gap) restricts its application as an active semiconducting component in most traditional electronic devices.[7,8] One approach to overcome this issue is to confine the electron delocalization in one dimension by forming graphene nanoribbons (GNRs), which opens a bandgap whose value is correlated with the width and edge configuration of the GNRs.[9–14] Over the past decade, several examples of soluble GNRs have been reported using a bottom-up approach to prepare well-defined GNRs with controlled edge structures.[15–20] In most cases, these GNRs are synthesized from polymeric precursors containing small aromatic units such as benzene, naphthalene,[21] and heterocycles (for doped GNRs)[19] bonded together to form the GNR backbone. Consequently, when wider GNRs are desired, monomers containing several aromatic units must be prepared. This process often involves multiple synthetic steps, making the overall synthesis labor-intensive and time-consuming. A potential solution to this challenge is the use of larger aromatic units with multiple fused rings as building blocks for the monomers. In this context, polycyclic aromatic hydrocarbons (PAHs) such as pyrene,[22] coronene,[23] and perylene[24] have been explored, leading to larger structures in fewer synthetic steps. However, examples of GNRs derived from large PAHs through solution-phase synthesis remain limited, highlighting the need for further investigation in this area.

Herein, we report the synthesis, characterization and device performances of new contorted GNRs, namely 2,9-dibromodibenzo[*b*,*def*]chrysene-7,14-dione (vat orange 1) and 4,10-dibromodibenzo[*def*,*mno*]chrysene-6,12-dione (vat orange 3, Fig. 1). We have shown in a previous report that annulation of these acenoacene scaffolds lead to contorted polycyclic aromatic hydrocarbons (PAHs), due the presence of two bulky substituents in the bay region.[25] Nonetheless, a significant decrease of the bandgap value was observed upon annulation, while maintaining excellent stability under ambient conditions. **GNR1** and **GNR2**, which can be regarded as polymeric version of these contorted PAHs, were prepared using the Brønsted acid-catalyzed alkyne benzannulation reaction developed by Swager and optimized by Chalifoux and coworkers for polycyclic aromatic hydrocarbons (PAHs) and GNRs.[26–28] The structural integrity of the GNRs was verified using various techniques including UV-visible absorption and nuclear magnetic resonance (NMR). The GNRs were also tested in field-effect transistors.

Results and discussion

Recently, we reported the highly regioselective alkyne benzannulation on vat orange 1 and 3 derivatives bearing alkoxy chains at the 7, 14 and 6, 12 positions, respectively (Fig. 2).[25] The methanesulfonic acid (MSA) catalyzed cyclization occurs under kinetic control at the more crowded positions, close to the alkoxy chains, causing the PAH scaffold to bend significantly.

[a] *Département de Chimie and Centre de Recherche sur les Matériaux Avancés (CERMA), 1045 Ave de la Médecine, Université Laval, Québec, QC, G1V 0A6, Canada. E-mail: jean-francois.morin@chm.ulaval.ca*

[b] *Department of Chemistry & Biochemistry, University of Windsor, Essex-Hall 375-1, Windsor, ON, N9B 3P4, Canada*

† Electronic supplementary information (ESI) available: Details of experimental procedures, ^{1}H NMR, ^{13}C NMR, UV-visible spectroscopy, conditions for each parameter of dispersion, IR spectroscopy, AFM, and DFT calculations (PDF). See DOI: https://doi.org/10.1039/d4tc05043f

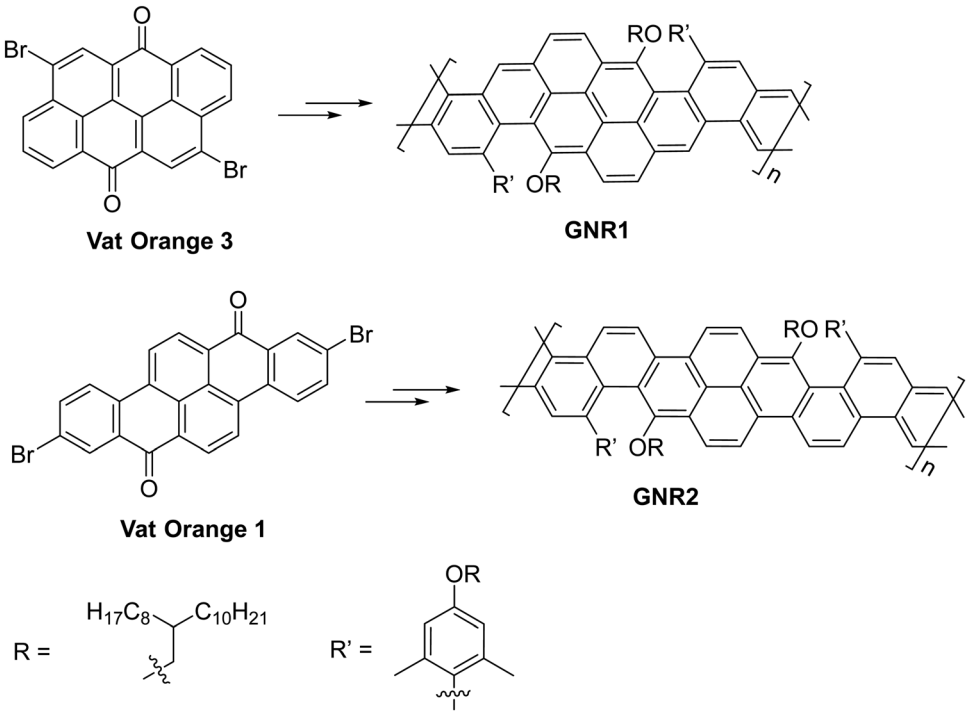

Fig. 1 Structures of **GNR1** and **GNR2** from vat orange 3 and vat orange 1.

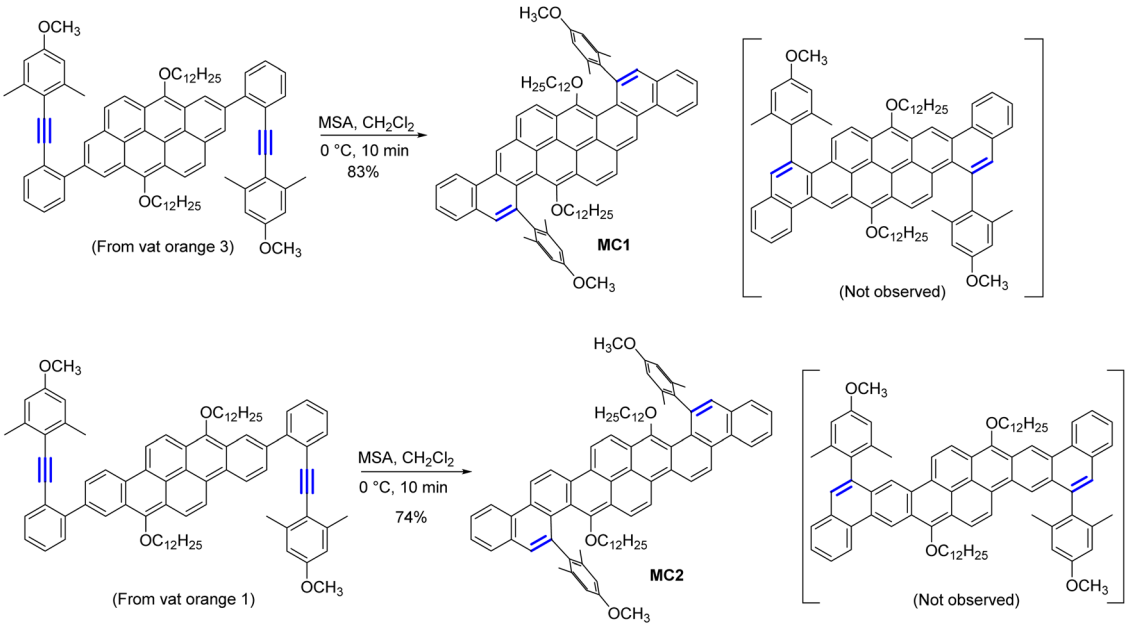

Fig. 2 Brønsted acid-catalyzed alkyne benzannulation on vat dye derivatives showing high regioselectivity towards the most sterically hindered positions. Adapted from ref. 25.

The cyclization was completed in less than 10 minutes and all the starting material was consumed. No trace of other isomers from cyclization at other possible positions was detected. This high regioselectivity on both vat orange 1 and vat orange 3 derivatives upon alkyne benzannulation indicates that these could be used as building blocks to prepare regioregular GNRs.

Synthesis of the GNRs

The synthesis of **GNR1** and **GNR2** is shown in Scheme 1. Starting from vat orange 3, a reduction-alkylation sequence was performed using a procedure previously optimized for vat orange 3.[29] A branched alkyl chain was used to ensure optimal solubility of the polymeric precursors and **GNRs.**

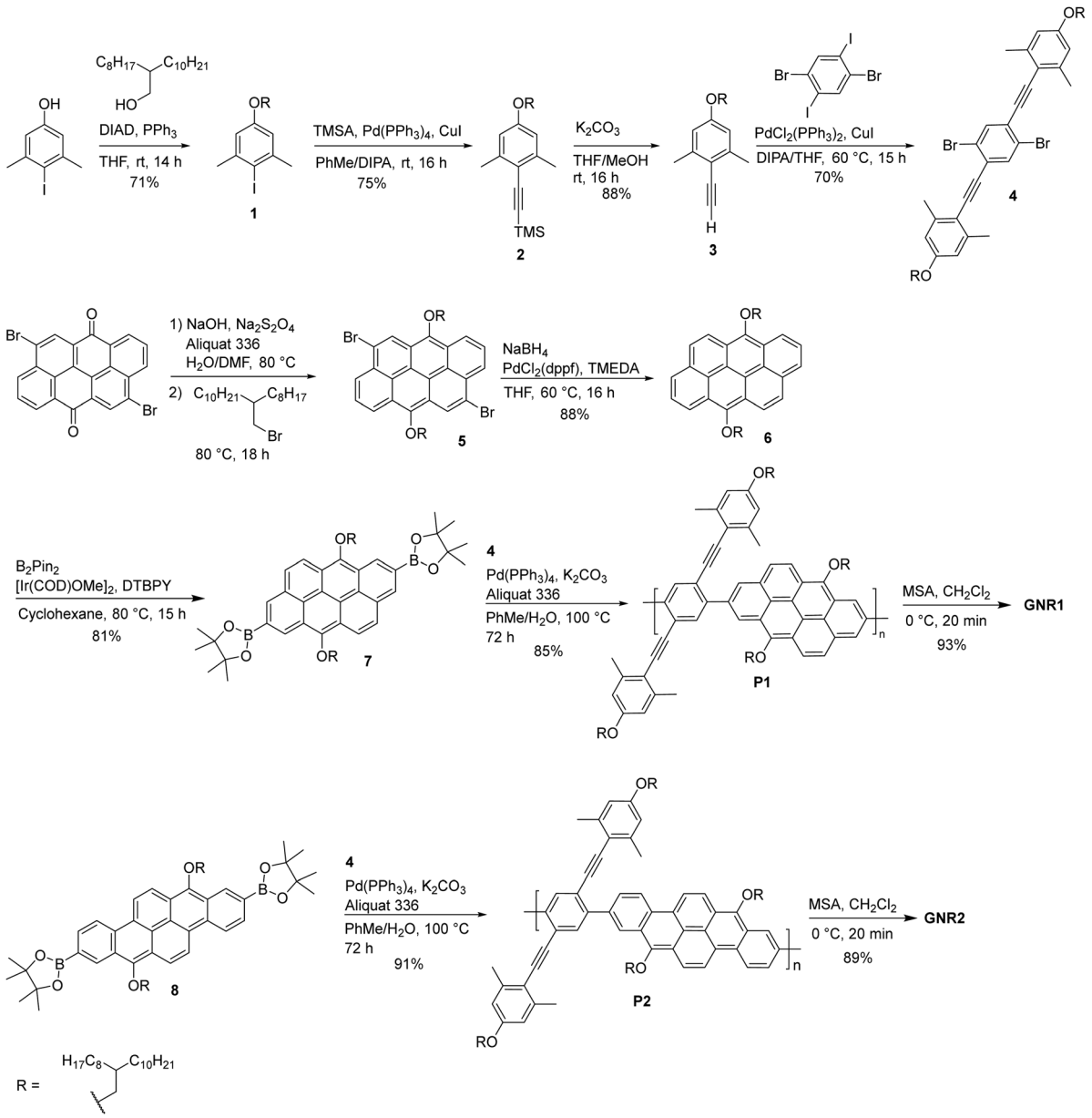

Scheme 1 Synthesis of **GNR1** and **GNR2**.

Then, a palladium-catalyzed debromination followed by an iridium-catalyzed borylation at the 2 and 8 positions were achieved to yield compound **7**. This compound was thus engaged in a Suzuki–Miyaura polymerization reaction with compound **4** (prepared following a reported protocol for a very similar molecule).[25] to provide **P1** in 85% yield. It is worth noticing that the presence of methyl groups in *ortho* position relative to the alkyne are not necessary for the alkyne benzannulation to proceed, but it prevents side reactions during the ring closure due to steric effect, ensuring high structural fidelity of the resulting GNR.[30] The polymer was thoroughly purified by precipitation in methanol, followed by washing with methanol and hexanes in a Soxhlet apparatus to removed catalyst residue and the low molecular weight fraction. Finally, **P1** was treated with methanesulfonic acid (MSA) in dichloromethane using the same conditions previously optimized for vat dyes.[25] Upon addition of MSA, the solution rapidly changed color, suggesting a very fast conversion of **P1** to **GNR1**. The color of the solution remained unchanged even after the addition of an excess amount of the acid. Interestingly, no precipitation was observed upon the formation of **GNR1** in dichloromethane at 0 °C. The good solubility of **GNR1** can be attributed not solely to the presence of long, branched alkyl chains, but also to the inherent twisted conformation of the GNR structure that makes π-stacking less effective. After 20 minutes, the mixture was neutralized and **GNR1** was recovered in 93% yield. The same synthetic sequence was used for the synthesis of **GNR2** by starting with compound **8** that has been previously reported by our group.[29] As **GNR1**, **GNR2** exhibit excellent solubility in common organic solvents.

Structural analysis and properties

^{1}H NMR spectra of both **GNR1** and **GNR2** and their polymeric precursors are shown in Fig. 3. The ^{1}H NMR analysis reveals the same patterns observed for pre- and post-cyclized model compounds (see Fig. 2). For **P1**, the two aromatic protons of the symmetrical pendant 2,6-dimethyl-4-methoxybenzene appear as one singlet at δ = 6.43 ppm (red dots, Fig. 3a), suggesting a freely rotating phenyl ring. Upon cyclization (Fig. 3b), this singlet splits into two distinct signals at δ = 7.11 and 6.20 ppm due to the constrained rotation of the phenyl facing a long, branched alkoxy chain in the bay region of **GNR1**. The complete disappearance of the peaks in the aromatic region between δ = 9.20 and 8.60 ppm along with the appearance of a new peak downfield at δ = 9.65 ppm suggest a complete benzannulation reaction. Similar observations can be made for going from **P2** to **GNR2** (Fig. 3c and d).

Infrared spectroscopy was performed on both GNRs polymers and their polymeric precursors to evaluate the disappearance of the band associated with the C≡C bond stretching after benzannulation. The findings are presented in Fig. S17 (ESI†). As expected, the FTIR spectrum of both polymers **P1** and **P2** displays a peak at 2199 cm^{-1}, whereas this peak almost completely disappears for **GNR1** and **GNR2**, indicating an almost complete benzannulation reaction. However, our attempt to perform Raman spectroscopy was unsuccessful as we were unable to observe the spectra of the polymers and GNRs due to significant fluorescence from both GNRs.

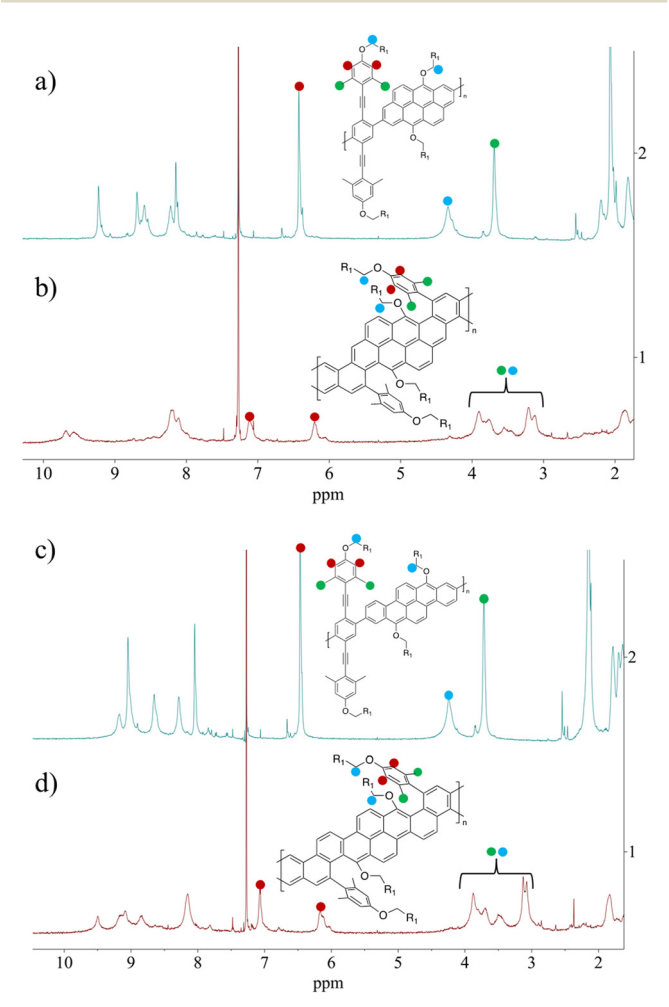

Fig. 3 ^{1}H NMR spectra of (a) **P1**, (b) **GNR1**, (c) **P2** and (d) **GNR2** in $CDCl_3$.

The molecular weight values (M_n and M_w) of **P1**, **P2**, **GNR1** and **GNR2** were determined using size exclusion chromatography (SEC), employing polystyrene standards and 1,2,4-trichlorochlorobenzene as the eluent at 110 °C. The results are presented in Table 1.

The degree of polymerization (X_n) for both **P1** and **P2** are similar at 13 and 15, respectively. Interestingly, upon cyclization, the M_n values of both GNRs remain relatively the same, meaning that the rigidification of the structures did not result in a significant change in their hydrodynamic volume.

The photophysical properties of the GNRs and their polymeric precursors **P1** and **P2** have been determined by UV-visible and fluorescence spectroscopy and the results are summarized in Table 2 and Fig. 4. Upon benzannulation on **P1** to yield **GNR1**, an important red-shift of 160 nm (from 470 to 630 nm) was observed, indicative of a significant extension of the effective conjugation length. Interestingly, the benzannulation on **P2**, which has a similar λ_{max} value (470 and 456 nm for **P1** and **P2** in chloroform, respectively) did not produce such a significant red shift (44 nm). This can be explained in part by the increased lateral conjugation (larger GNR width) for **GNR1** compared to **GNR2**. For both **GNR1** and **GNR2**, the absorption band features a vibronic structure similar to that of their precursor, indicating a well-defined structure. Moreover, the solid-state spectrum of **GNR1** and **GNR2** are slightly red shift (2 nm for both) compared to the solution state, suggesting that the GNRs structure are rigid and that no significant π–π stacking is taking place in the solid state. Finally, **GNR2** exhibits a featureless emission band in the visible region with a λ_{emi} value of 585 nm, while **GNR1** exhibit an intense peak centered at λ_{emi} 643 nm with a shoulder at *ca.* 700 nm, which can be assigned as a vibronic band. The small Stokes shift value (13 and 34 nm for **GNR1** and **GNR2**, respectively) is another indication of the rigid nature of the conjugated backbone. The photophysical properties of **GNR1** and **GNR2** were also compared to their model compounds (Fig. 2).[25] **GNR1** and **GNR2** are red shifted by 85 and 45 nm compared to **MC1** and **MC2**, respectively.

Table 1 Molecular weight values and dispersity index of **P1**, **P2**, **GNR1** and **GNR2**

Polymer	M_n (kg mol^{-1})	M_w[a] (kg mol^{-1})	$Đ$[a] (M_n/M_w)	X_n
P1	23	59	2.5	13
P2	27	86	3.1	15
GNR1	24	48	2.0	13
GNR2	27	81	3.0	15

M_n represents the number average molecular weight, $\overline{M_w}$ indicate the weight average molecular weight, and $Đ$ denotes the dispersity index. [a] The molecular weight and $Đ$ values for **P1** and **P2** were determined by size exclusion chromatography (SEC) at 135 °C. This involved utilizing 1,2,4-trichlorobenzene as the eluent and employing polystyrene as the standard for measurement.

Table 2 Photophysical and electrochemical properties of polymers and their counterpart GNRs

	λ_{max}^{sol} [a] [nm]	λ_{max}^{film} [a] [nm]	λ_{onset}^{sol} [b] [nm]	$E_{optical}$ [c] [eV]	λ_{Emis} [d] [nm]	ϕ_F [e] [%]	E_{HOMO} [f] [eV]
P1	470	N/A	490	2.53	N/A	—	N/A
GNR1	630	632	655	1.89	643	10	−4.67
P2	456	N/A	504	2.46	N/A	—	N/A
GNR2	551	553	576	2.15	585	33	−4.74

[a] Absorption wavelengths of the lowest energies. [b] Estimated from the onset of the UV-vis spectra. [c] Calculated at the λ_{onset}. [d] The λ_{max} of the emission spectra. [e] Calculated according to $E_{HOMO} = -[(E_{ox\ vs.\ Ag/Ag^+}) - (E_{ferrocene\ vs.\ Ag/Ag^+}^{1/2}) + 4.8]$ from the electrochemical measurements performed in the thin fil state. All optical measurements in solution have been performed in chloroform. [f] The quantum yield have been measured in CH_2Cl_2 using cresyl violet perchlorate (560 nm) (ϕ_F = 54 in MeOH) for **GNR1** and rhodamine B (510 nm) (ϕ_F = 70 in EtOH) for **GNR2** as the standards.

To get insights on the electronic properties of both GNRs, DFT calculations were performed on oligomers (two repeated units) using B3LYP/6-31+G(d,p) using Gaussian[31] to determine the frontiers orbitals distribution and energy (Fig. S29, ESI†). The calculated bandgap of **GNR1** (2.10 eV) is smaller than that of **GNR2** one (2.34 eV), which agrees with the experimental results suggesting a higher bandgap for **GNR2** than for **GNR1**.

Differential scanning calorimetry (DSC) and thermogravimetric analysis (TGA) were utilized to measure the thermal properties, and the corresponding results can be found in Fig. S18 and S19 (ESI†), respectively. The DSC analysis did not indicate a distinct glass transition temperature (T_g) nor a fusion transition. Consequently, it can be inferred that the GNRs are amorphous. TGA analyses were conducted under a nitrogen atmosphere at a heating rate of 10 °C per minute. The decomposition temperature (T_d) values, determined at 5% weight loss, are 310 °C and 270 °C for **GNR1** and **GNR2**, respectively.

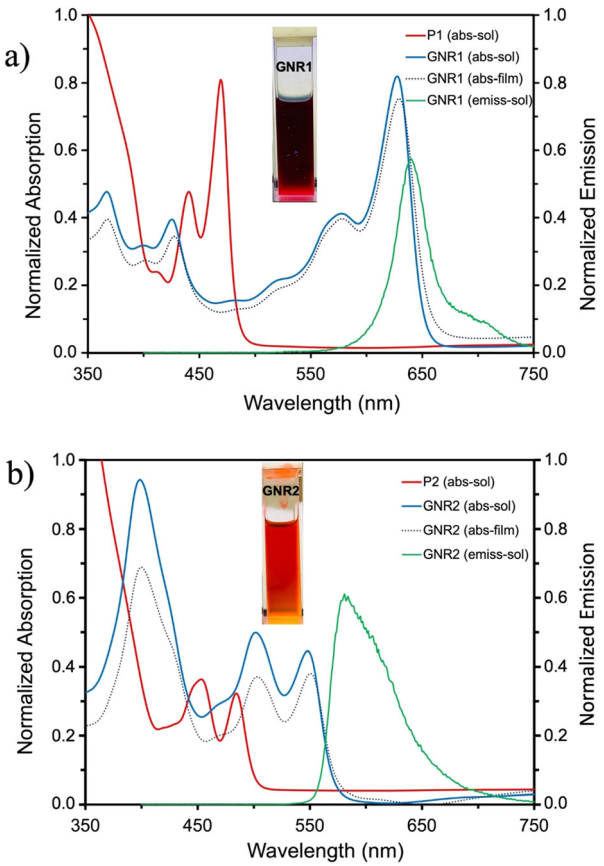

Fig. 4 UV-visible absorption and emission (in chloroform for solution measurements) spectra of (a) **P1** and **GNR1**, (b) **P2** and **GNR2**.

GNRs for OFET application

GNR1 and **GNR2** were used as active layers in organic field-effect transistors (OFETs) to evaluate their electronic properties. Bottom-gate top-contact devices were fabricated using solution deposition *via* spin-coating of **GNR1** and **GNR2** in toluene and 2-methyl tetrahydrofuran (2-MeTHF), with the experimental procedure detailed in the OFET device section in the ESI.† Both solvents are explored for specific reasons – toluene is a commonly used high-boiling point solvent for OFET fabrication, while 2-MeTHF offers a greener alternative with lower toxicity and environmental impact. Briefly, the polymers were dissolved in the selected solvent at a concentration of 5 mg mL^{-1} and stirred at 70 °C for 1 hour before spin-coating at 1000 rpm onto OTS-modified doped Si/SiO_2 substrates.[32] The coated substrates were then annealed at 150 °C for 30 minutes in an N_2 glovebox. Gold electrodes were deposited through physical vapor deposition. Transfer and output curves were measured in a N_2 glovebox for all devices, with representative curves shown in Fig. S25 and S26 (ESI†). The charge carrier mobility was extracted from the transfer curves through linear fitting of $I_{DS}^{1/2}$ *vs.* V_{GS} in the saturation regime using $I_{DS(sat)} = (WC/2L)\mu_{sat}(V_G - V_{th})^2$. Since some of the transfer curves exhibited slight non-linearity, a slope of $I_{DS}^{1/2}$ *vs.* V_{GS} from approximately V_{GS} = −15 V to −55 V was used to avoid over- or underestimation of mobilities (shown as dotted lines in Fig. S25, ESI†). The results obtained from the fabricated OFETs are summarized in Table 3.

The devices fabricated from **GNR1** exhibited good hole mobilities, with a maximum average of 1.34×10^{-2} $cm^2\ V^{-1}\ s^{-1}$ when processed in toluene. The polymer also demonstrated high $I_{ON/OFF}$ (10^5) values and low threshold voltages. Although the average mobilities for **GNR2** were slightly lower (1.22×10^{-2} $cm^2\ V^{-1}\ s^{-1}$ in toluene) and the devices showed slightly higher threshold voltages, the performance was still comparable to that of **GNR1**. Interestingly, both nanoribbons showed improved performance when processed from toluene compared to 2-MeTHF, which can be attributed to the combination of a slightly lower solubility in this solvent and increased surface roughness in thin films. Nonetheless, **GNR1** and **GNR2** both demonstrated good solubility and film formation when processed from toluene and 2-MeTHF.

Table 3 Average and maximum hole mobilities (μ_h^{ave}/μ_h^{max}), threshold voltages (V_{th}), and I_{on}/I_{off} current ratios for OFETs fabricated from **GNR1** and **GNR2** processed in toluene and 2-methyl tetrahydrofuran. Results are averaged from a minimum of 7 devices, and acquired after thermal annealing at 150 °C

GNR	Solvent	μ_h^{ave}/μ_h^{max} [$cm^2\ V^{-1}\ s^{-1}$]	I_{ON}/I_{OFF}^{ave}	V_{th}^{ave} [V]
GNR1	Toluene	0.013 ± 0.001/0.015	10^5	−3.9
GNR1	2-MeTHF	0.007 ± 0.001/0.008	10^5	−2.6
GNR2	Toluene	0.012 ± 0.003/0.015	10^5	−5.7
GNR2	2-MeTHF	0.008 ± 0.001/0.010	10^4	−7.2

This is particularly noteworthy given that graphene nanoribbons are often insoluble due to strong π–π interactions and typically require additional chemical functionalization to access solution deposition methods which can disrupt their charge transport properties.[33] Given that GNRs can often only be processed in devices from chemical vapor deposition or on-surface synthesis (both costly and not easily scalable methods), this feature is particularly promising for printed electronics. It is also important to note that the favorable device characteristics obtained from thin film formation in a non-halogenated solvent like 2-MeTHF (more eco-friendly alternatives to common halogenated solvents) open new avenues toward a scalable and sustainable fabrication manufacturing of GNR-based OFETs.[34,35]

To gain deeper insights into the properties of GNR1 and GNR2 in thin film, atomic force microscopy (AFM) was used to evaluate the nanoscale morphology in the solid state. This technique was used not only to examine the influence of chemical design on thin film nanostructure, but also to assess the impact of the processing solvent (toluene or 2-MeTHF) on thin film properties and OFET performance. As shown in Fig. S27 and S28 (ESI†), films of both GNRs processed from toluene exhibited smooth surfaces, without large aggregates. An RMS roughness of 1.73 and 1.16 nm was measured for GNR1 and GNR2, respectively, when processed from toluene. In contrast, thin film of GNR1 prepared using 2-MeTHF displayed significantly higher roughness (RMS = 14.9 nm) and the presence of large aggregated was observed by AFM. This result can be attributed to the higher polarity and lower boiling point of 2-MeTHF, which can promote aggregation upon solution deposition. Similar observations have been reported in previous studies utilizing polar solvents for semiconducting polymers thin film formation.[36,37] For GNR2, the impact of processing in 2-MeTHF on aggregation is significantly less pronounced compared to GNR1, with only a minimal increase in surface roughness. This difference can be attributed to the superior solubility of GNR2 in 2-MeTHF relative to GNR1. Overall, the increased surface roughness provides a partial explanation for the reduced OFET performance observed for both GNRs when processed from 2-MeTHF.

Conclusion

In conclusion, two twisted graphene nanoribbons (GNRs) were synthesized in a few synthetic steps from readily available, low-cost vat orange 1 and vat orange 3, utilizing a Brønsted acid-catalyzed alkyne benzannulation reaction. These highly soluble GNRs, with bandgap values around 2.0 eV, were incorporated as active layers in organic field-effect transistors (OFETs) to assess their electronic properties. Achieving hole mobilities of up to 1.34×10^{-2} $cm^2\ V^{-1}\ s^{-1}$, these GNRs demonstrate promising potential for printed electronics. Notably, they can be processed from eco-friendly 2-MeTHF and exhibit favorable charge transport properties, highlighting their suitability for sustainable electronic device fabrication.

Data availability

Additional data supporting this article have been uploaded as part of the ESI.†

Conflicts of interest

There are no conflicts to declare.

Acknowledgements

J.-F. Morin and S. R.-G. thank the Natural Sciences and Engineering Research Council of Canada (NSERC) for support through a Discovery Grants (RGPIN-2019-04215 and RGPIN-2022-04428). M. M. and F. G. thank NSERC for financial support through a Canada Postgraduate Scholarship – Doctoral (PGS-D).

References

1 A. K. Geim, *Science*, 2009, **324**, 1530–1534.
2 A. K. Geim and K. S. Novoselov, *Nat. Mater.*, 2007, **6**, 183–191.
3 A. A. Balandin, *Nat. Mater.*, 2011, **10**, 569–581.
4 Y. Xu, Z. Li and W. Duan, *Small*, 2014, **10**, 2182–2199.
5 K. S. Novoselov, Z. F. Jiang, Y. S. Zhang, S. V. Morozov, H. L. Stormer, U. Zeitler, J. C. Maan, G. S. Boebinger, P. Kim and A. K. Geim, *Science*, 2007, **315**, 1379.
6 Y. Zhang, Y. W. Tan, H. L. Stormer and P. Kim, *Nature*, 2005, **438**, 201–204.
7 L. Zhang, Y. Cao, N. S. Colella, Y. Liang, J. L. Brédas, K. N. Houk and A. L. Briseno, *Acc. Chem. Res.*, 2015, **48**, 500–509.
8 J. Mei, Y. Diao, A. L. Appleton, L. Fang and Z. Bao, *J. Am. Chem. Soc.*, 2013, **135**, 6724–6746.
9 D. Moran, F. Stahl, H. F. Bettinger, H. F. Schaefer and P. V. R. Schleyer, *J. Am. Chem. Soc.*, 2003, **125**, 6746–6752.
10 K. Nakada, M. Fujita, G. Dresselhaus and M. S. Dresselhaus, *Phys. Rev. B: Condens. Matter Mater. Phys.*, 1996, **54**, 17954.
11 M. R. Philpott and Y. Kawazoe, *J. Chem. Phys.*, 2011, **134**, 124706.
12 S. Fujii and T. Enoki, *Acc. Chem. Res.*, 2013, **46**, 2202–2210.
13 T. Enoki, Y. Kobayashi and K. I. Fukui, *Int. Rev. Phys. Chem.*, 2007, **26**, 609–645.

14 M. Kastler, J. Schmidt, W. Pisula, D. Sebastiani and K. Müllen, *J. Am. Chem. Soc.*, 2006, **128**, 9526–9534.
15 W. Yang, A. Lucotti, M. Tommasini and W. A. Chalifoux, *J. Am. Chem. Soc.*, 2016, **138**, 9137–9144.
16 Y. L. Lee, F. Zhao, T. Cao, J. Ihm and S. G. Louie, *Nano Lett.*, 2018, **18**, 7247–7253.
17 J. Liu, B. W. Li, Y. Z. Tan, A. Giannakopoulos, C. Sanchez-Sanchez, D. Beljonne, P. Ruffieux, R. Fasel, X. Feng and K. Müllen, *J. Am. Chem. Soc.*, 2015, **137**, 6097–6103.
18 M. Daigle, D. Miao, A. Lucotti, M. Tommasini and J.-F. Morin, *Angew. Chem., Int. Ed.*, 2017, **56**, 6213–6217.
19 D. Miao, M. Daigle, A. Lucotti, J. Boismenu-Lavoie, M. Tommasini and J.-F. Morin, *Angew. Chem., Int. Ed.*, 2018, **57**, 3588–3592.
20 C. Tao, L. Jiao, O. V. Yazyev, Y. C. Chen, J. Feng, X. Zhang, R. B. Capaz, J. M. Tour, A. Zettl, S. G. Louie, H. Dai and M. F. Crommie, *Nat. Phys.*, 2011, **7**, 616–620.
21 A. Keerthi, C. Sánchez-Sánchez, O. Deniz, P. Ruffieux, D. Schollmeyer, X. Feng, A. Narita, R. Fasel and K. Müllen, *Chem. – Asian J.*, 2020, **15**, 3807–3811.
22 S. Obermann, W. Zheng, J. Melidonie, S. Böckmann, S. Osella, N. Arisnabarreta, L. A. Guerrero-León, F. Hennersdorf, D. Beljonne, J. J. Weigand and M. Bonn, *Chem. Sci.*, 2023, **14**, 8607–8614.
23 Y. Kinno, H. Omachi and H. Shinohara, *Appl. Phys. Express*, 2019, **13**, 015002.
24 S. R. Peurifoy, Q. Xu, R. May, N. A. Gadjieva, T. J. Sisto, Z. Jin, L. E. Marbella and C. Nuckolls, *Chem. Sci.*, 2020, **11**, 9978–9982.
25 A. Darvish, F. Lirette, I. Fernández and J.-F. Morin, *Chem. – Eur. J.*, 2024, e202403456.
26 W. Yang and W. A. Chalifoux, *Synlett*, 2017, 625–632.
27 M. B. Goldfinger and T. M. Swager, *J. Am. Chem. Soc.*, 1994, **116**, 7895–7896.
28 M. B. Goldfinger, K. B. Crawford and T. M. Swager, *J. Am. Chem. Soc.*, 1997, **119**, 4578–4593.
29 F. Gagnon, V. Tremblay, A. Soldera, M. U. Ocheje, S. Rondeau-Gagné, M. Leclerc and J.-F. Morin, *Mater. Adv.*, 2022, **3**, 599–603.
30 W. Zheng, T. Ikai and E. Yashima, *Angew. Chem., Int. Ed.*, 2021, **133**, 11394–11399.
31 M. J. Frisch, G. W. Trucks, H. B. Schlegel, G. E. Scuseria, M. A. Robb, J. R. Cheeseman, G. Scalmani, V. Barone, G. A. Petersson, H. Nakatsuji, X. Li, M. Caricato, A. V. Marenich, J. Bloino, B. G. Janesko, R. Gomperts, B. Mennucci, H. P. Hratchian, J. V. Ortiz, A. F. Izmaylov, J. L. Sonnenberg, L. Williams, F. Ding, F. Lipparini, F. Egidi, J. Goings, B. Peng, A. Petrone, T. Henderson, D. Ranasinghe, V. G. Zakrzewski, J. Gao, N. Rega, G. Zheng, W. Liang, M. Hada, M. Ehara, K. Toyota, R. Fukuda, J. Hasegawa, M. Ishida, T. Nakajima, Y. Honda, O. Kitao, H. Nakai, T. Vreven, K. Throssell, J. A. Montgomery Jr., J. E. Peralta, F. Ogliaro, M. J. Bearpark, J. J. Heyd, E. N. Brothers, K. N. Kudin, V. N. Staroverov, T. A. Keith, R. Kobayashi, J. Normand, K. Raghavachari, A. P. Rendell, J. C. Burant, S. S. Iyengar, J. Tomasi, M. Cossi, J. M. Millam, M. Klene, C. Adamo, R. Cammi, J. W. Ochterski, R. L. Martin, K. Morokuma, O. Farkas, J. B. Foresman and D. J. Fox, *Gaussian 09, Revision D.01*, Gaussian Inc., Wallingford, CT, 2016.
32 Y. Ito, A. A. Virkar, S. Mannsfeld, H. O. Joon, M. Toney, J. Locklin and Z. Bao, *J. Am. Chem. Soc.*, 2009, **131**, 9396–9404.
33 B. Genorio and A. Znidarsic, *J. Phys. D: Appl. Phys.*, 2014, **47**, 094012.
34 C. M. Alder, J. D. Hayler, R. K. Henderson, A. M. Redman, L. Shukla, L. E. Shuster and H. F. Sneddon, *Green Chem.*, 2016, **18**, 3879–3890.
35 C. S. Slater, M. J. Savelski, D. Hitchcock and E. J. Cavanagh, *J. Environ. Sci. Health, Part A*, 2016, **51**, 487–494.
36 M. Mooney, Y. Wang, A. Nyayachavadi, S. Zhang, X. Gu and S. Rondeau-Gagné, *ACS App. Mater. Interfaces.*, 2021, **13**, 25175–25185.
37 M. Mooney, A. Nyayachavadi, A. Awada, E. Iakovidis, Y. Wang, M. N. Chen, Y. Liu, J. Xu, Y. C. Chiu, X. Gu and S. Rondeau-Gagné, *Polym. Chem.*, 2023, **14**, 562–572.